CrossMark

The Missing Link of Sulfur Chemistry in TMC-1: The Detection of c-C$_3$H$_2$S from the GOTHAM Survey

Anthony J. Remijan[1] , P. Bryan Changala[2] , Ci Xue[3] , Elsa Q. H. Yuan[4] , Miya Duffy[3], Haley N. Scolati[5,8] ,
Christopher N. Shingledecker[6] , Thomas H. Speak[4] , Ilsa R. Cooke[4] , Ryan Loomis[1] , Andrew M. Burkhardt[7] ,
Zachary T. P. Fried[3] , Gabi Wenzel[2,3] , Andrew Lipnicky[1] , Michael C. McCarthy[2] , and Brett A. McGuire[1,3]
[1] National Radio Astronomy Observatory, Charlottesville, VA 22903, USA
[2] Center for Astrophysics | Harvard & Smithsonian, Cambridge, MA 02138, USA
[3] Department of Chemistry, Massachusetts Institute of Technology, Cambridge, MA 02139, USA
[4] Department of Chemistry, University of British Columbia, 2036 Main Mall, Vancouver, BC V6T 1Z1, Canada
[5] Department of Chemistry, University of Virginia, Charlottesville, VA 22904, USA
[6] Department of Chemistry, Virginia Military Institute, Lexington, VA 24450, USA
[7] Department of Earth, Environment, and Physics, Worcester State University, Worcester, MA 01602, USA

Abstract

We present the spectroscopic characterization of cyclopropenethione in the laboratory and detect it in space using the Green Bank Telescope Observations of TMC-1: Hunting Aromatic Molecules survey. The detection of this molecule—the missing link in understanding the C$_3$H$_2$S isomeric family in TMC-1—completes the detection of all three low-energy isomers of C$_3$H$_2$S, as both CH$_2$CCS and HCCCHS have been previously detected in this source. The total column density of this molecule (N_T of $5.72^{+2.65}_{-1.61} \times 10^{10}$ cm^{-2} at an excitation temperature of $4.7^{+1.3}_{-1.1}$ K) is smaller than both CH$_2$CCS and HCCCHS and follows nicely the relative dipole principle (RDP), a kinetic rule of thumb for predicting isomer abundances that suggests that, all other chemistry among a family of isomers being the same, the member with the smallest dipole (μ) should be the most abundant. The RDP now holds for the astronomical abundance ratios of both the S-bearing and O-bearing counterparts observed in TMC-1; however, CH$_2$CCO continues to elude detection in any astronomical source.

Unified Astronomy Thesaurus concepts: Astrochemistry (75); Chemical abundances (224)

Materials only available in the online version of record: tar.gz files

1. Introduction

Sulfur is one of the more abundant elements in the interstellar medium (ISM), rounding out the top 10 most abundant molecules with an abundance of $\sim 10^{-5}$ with respect to hydrogen (M. Asplund et al. 2005; J. C. Howk et al. 2006). Sulfur-bearing molecules offer valuable diagnostics into the physical and chemical properties of astronomical regions (see, e.g., S. B. Charnley 1997; P. Stäuber et al. 2005; G. B. Esplugues et al. 2014; P. Gorai et al. 2024, and references therein). For instance, small diatomic molecules like CS are commonly used as "dense gas tracers" because they are typically found in regions of higher extinction—where gas and dust densities are elevated—and are less readily detected in lower-density regions dominated by CO (see, e.g., S. Zhou et al. 1993). Similarly, SO and SO$_2$ are often considered "shock tracers," as they are frequently associated with protostellar jets of material ejected by newly forming stars (G. B. Esplugues et al. 2014; E. Artur de la Villarmois et al. 2023).

However, it remains unclear what process (or processes) drive the production of these sulfur-bearing species in the wide variety of astronomical environments. Are physical conditions alone sufficient to account for their selective detection, or is it a combination of both physical and chemical factors? For example, CS is now consistently observed in both diffuse and dense gas (M. Gerin et al. 2024), and SO$_2$ can be found in the cold molecular envelopes of hot core regions just as readily as in shock-heated gas (e.g., Ł. Tychoniec et al. 2021). From a chemical perspective, it is also intriguing to explore how the abundances and formation pathways of S-containing molecules compare to their oxygen-bearing counterparts, as oxygen and sulfur exhibit similar electron configurations, with six valence electrons that enable them to form two covalent bonds in neutral molecules.

Effectively probing these chemical formation and destruction pathways requires controlled tests where the effects of variables not of interest are minimized. To this end, observations of families of molecular isomers are particularly powerful (see, e.g., C. Xue et al. 2019, and references therein). Recent interest has been drawn to the C$_3$H$_2$O isomeric family of molecules in order to test the relative influence of kinetic versus thermodynamic control (J.-C. Loison et al. 2016). Notably, the most stable isomer, propadienone (CH$_2$CCO), remains undetected in astronomical sources, while its higher-energy structural isomers, propynal (HCCCHO) and cyclopropenone (c-C$_3$H$_2$O), have been known and studied for decades (W. M. Irvine et al. 1988; J. M. Hollis et al. 2006; R. A. Loomis et al. 2015; J.-C. Loison et al. 2016; C. N. Shingledecker et al. 2019). This raises important questions: Do we fully understand the chemical formation pathways responsible for this discrepancy? Moreover, why has HCCCHO exclusively been detected in extremely cold regions (temperatures below 10 K), while evading detection in both high- and low-mass hot molecular cores?

[8] Currently a Grote Reber Fellow of the National Radio Astronomy Observatory.

Even more curious is the recent detection of the S-analog of this species toward TMC-1—propadienethione (CH_2CCS) (J. Cernicharo et al. 2021a). High-sensitivity spectral line observations of TMC-1 were performed using the Yebes 40 m telescope as part of the *Q*-band Ultrasensitive Inspection Journey to the Obscure TMC-1 Environment (QUIJOTE) survey (J. Cernicharo et al 2022). From these observations, CH_2CCS was identified with a total column density of $(3.7 \pm 0.4) \times 10^{11}$ cm^{-2} and a derived rotational temperature of 10 ± 1 K. The ortho/para ratio was also measured to be 4.6 ± 0.8, consistent with the canonical value of 3:1 expected from the statistical spin degeneracies (K. M. Yocum et al. 2023). The HCCCHS isomer was previously detected by J. Cernicharo et al. (2021b) also as part of the QUIJOTE survey, where a total column density of $(3.2 \pm 0.4) \times 10^{11}$ cm^{-2} was determined assuming a rotational temperature of 5 K. Thus, the relative column density ratio between these two isomers approaches ~ 1, significantly different from the upper limit to the column density ratio of $< 3\%$ between CH_2CCO and HCCCHO (J.-C. Loison et al. 2016).

Although the sulfur depletion problem remains a puzzle of the chemistry in dense clouds (D. P. Ruffle et al. 1999; T. H. G. Vidal et al. 2017; A. Fuente et al. 2023), the claim by J. Cernicharo et al. (2021a) that the dark cloud region TMC-1 is a "chemical factory for S-bearing molecules" is well justified because many additional S-bearing species have been detected toward TMC-1 that have not yet been identified in any other astronomical environment. In addition, the column densities of some S-bearing species are higher compared to their O-bearing analogs (see J. Cernicharo et al. 2021b, and references therein). Yet why are some of the S-species so prevalent compared to the O-species in this source, and what makes the environment of TMC-1 so unique to form the complex S-bearing species? These questions underscore the need to refine our understanding of the relative contribution between physical and chemical processes in determining what molecules are observed in astronomical sources.

To this end, cyclopropenethione (c-C_3H_2S) is a missing link in understanding the C_3H_2S isomeric family in TMC-1. Spectroscopic work on the C_3H_2S isomers, specifically HCCCHS and CH_2CCS, was first published in the 1980s (R. D. Brown et al. 1982, 1988), yet no experimental spectroscopy of c-C_3H_2S has been reported until the present work. Only recently have theoretical studies aimed at characterizing its geometry and other spectroscopic properties, such as the rotational partition function, been conducted (X. Song et al. 2022).

In this paper, we present the spectroscopic characterization of c-C_3H_2S both in the laboratory and in space and make the astronomical detection using the Green Bank Telescope (GBT) Observations of TMC-1: Hunting Aromatic Molecules (GOTHAM) survey. Section 2 describes the theoretical predictions used to determine the initial rotational constants of this molecule and the laboratory observations that led to its astronomical detection. Section 3 presents the observational details of the GOTHAM large program. Section 4 presents the results of the astronomical detection of c-C_3H_2S, Section 5 discusses the detection of c-C_3H_2S in the context of the detections of the other S-bearing species detected toward TMC-1 and their O-bearing analogs, and finally Section 6 summarizes our conclusions.

Table 1
The Theoretical CCSD(T) Structural Parameters and Spectroscopic Constants of c-C_3H_2 ^{32}S

Parameter	cc-pCVDZ	cc-pCVTZ	cc-pCVQZ	cc-pCV5Z
$r(C_1S)$ (Å)	1.634365	1.619490	1.616091	1.615162
$r(C_1C_2)$ (Å)	1.447876	1.426873	1.421809	1.420597
$r(C_2H)$ (Å)	1.092800	1.077818	1.076477	1.076160
$\theta(SC_1C_2)$ (deg)	152.124	152.099	152.069	152.062
$\theta(HC_2C_1)$ (deg)	150.540	150.175	150.096	150.063
μ_e (D)[a]	4.146	4.427	4.549	4.572
A_e (MHz)[b]	31313.58	32137.66	32273.07	32304.46
B_e (MHz)[b]	3971.54	4066.36	4089.65	4095.64
C_e (MHz)[b]	3524.52	3609.64	3629.70	3634.81
$A_e - A_0$ (MHz)[c]	172.74	175.69	⋯	⋯
$B_e - B_0$ (MHz)[c]	13.70	13.89	⋯	⋯
$C_e - C_0$ (MHz)[c]	16.23	16.55	⋯	⋯
D_J (kHz)[c]	0.466	0.495	⋯	⋯
D_K (kHz)[c]	55.094	58.203	⋯	⋯
D_{JK} (kHz)[c]	16.833	17.679	⋯	⋯
d_1 (Hz)[d]	−62.800	−66.162	⋯	⋯
d_2 (Hz)[d]	−20.569	−21.459	⋯	⋯

Note.
[a] The equilibrium electric dipole moment.
[b] The equilibrium rotational constants.
[c] The VPT2 ground-state vibrational corrections.
[d] The S-reduced (I^r) quartic CD parameters.

2. Spectroscopic Analysis

The laboratory search for the microwave spectrum of c-C_3H_2S was guided by high-level quantum chemical predictions of its spectroscopic parameters calculated with the CFOUR program package (D. A. Matthews et al. 2020; J. F. Stanton et al. 2020). The equilibrium geometry was optimized with coupled cluster theory including single, double, and perturbative triple excitations (CCSD(T); K. Raghavachari et al. 1989; R. J. Bartlett et al. 1990) using analytic gradient methods (T. J. Lee & A. P. Rendell 1991) and the Dunning correlation-consistent polarized core-valence basis sets (cc-pCVXZ, with X = D, T, Q, 5; T. H. Dunning 1989; D. E. Woon & T. H. Dunning 1995; K. A. Peterson & T. H. Dunning 2002), correlating all electrons except the sulfur 1 s inner-core electrons. The optimized structural parameters, equilibrium rotational constants, and electric dipole moments are summarized in Table 1. Cubic force fields computed with the cc-pCVDZ and cc-pCVTZ basis sets and finite differences of analytic gradients were used to derive the harmonic centrifugal distortion (CD) parameters and anharmonic vibrational zero-point corrections with second-order vibrational perturbation theory (VPT2; I. M. Mills 1972) (see Table 1). The best-estimate ground-state rotational constants, which combine the CCSD(T)/cc-pCV5Z equilibrium geometry with the CCSD(T)/cc-pCVTZ vibrational corrections, are $A_0 = 32128.77$, $B_0 = 4081.75$, and $C_0 = 3618.26$ MHz.

The microwave spectrum of c-C_3H_2S was measured with two cavity Fourier transform microwave (FTMW) spectrometers operating over 5–26 GHz and 5–40 GHz, respectively, coupled to supersonic electric discharge expansion sources (J. U. Grabow et al. 2005; K. N. Crabtree et al. 2016), an

approach previously used in our laboratory to produce a diverse array of other reactive S-bearing molecules (V. D. Gordon et al. 2001, 2002; M. C. McCarthy et al. 2003; K. L. K. Lee et al. 2019; B. A. McGuire et al. 2018). Dilute mixtures of a hydrocarbon precursor (0.1% HCCH) and a sulfur source (either 0.1% CS_2 or H_2S) were prepared in neon and expanded through a pulsed solenoid valve into a large vacuum chamber containing a Fabry–Pérot microwave cavity. Before expanding into the cavity, the gas mixture passed through two copper ring electrodes spaced by ∼1 cm and held at an electric potential difference of 0.8–1.2 kV, which generated an electric discharge (30 mA peak current) during the ∼300–600 μs gas pulse. The mixture supersonically expanded along the axis of the microwave cavity and cooled to an internal rotational temperature of approximately 2 K.

An initial laboratory search for c-C_3H_2S was performed using discharge expansion conditions optimized for the production of propadienethione, ℓ-C_3H_2S, a lower-energy chain isomer of c-C_3H_2S (R. D. Brown et al. 1988; M. C. McCarthy et al. 2021). We first targeted the $J_{K_a,K_c} = 2_{1,2} - 1_{1,1}$ transition of c-C_3H_2S, which was predicted to lie near 14936 MHz based on the best-estimate theoretical rotational constants. Six molecular features were detected within a ±30 MHz window centered around the predicted transition frequency, but only one (at 14931.538(2) MHz) could possibly be assigned to c-C_3H_2S: this line was observed only when the discharge was enabled; was not observed when HCCH, CS_2, or H_2S was removed; and was unaffected by an applied magnetic field, indicating a closed-shell species. A candidate for the $2_{1,1}$–$1_{1,0}$ transition predicted to lie near 15,863 MHz was subsequently detected at 15,857.989(2) MHz and passed the same series of tests. After a preliminary fit of the B and C rotational constants based on these two tentative assignments, 15 additional transitions were detected, totaling 17 lines between 7 and 40 GHz. The measured rest frequencies were reproduced to within the experimental uncertainty (2 kHz) by adjusting the three rotational constants (A, B, and C) and two quartic CD constants (D_J and D_{JK}), leaving the remaining CD constants fixed to their CCSD(T)/cc-pCVTZ theoretical values. Watson's S-reduced Hamiltonian (I^r representation) was used because c-C_3H_2S is near the prolate top limit. The laboratory rest frequencies and derived spectroscopic constants are summarized in Tables 2 and 3, respectively.

The experimentally derived rotational constants of c-C_3H_2S differ from the best-estimate theoretical predictions by less than 0.04%. Taken together with the experimental tests described above, the newly detected molecule would almost certainly be c-C_3H_2S, but definitive confirmation of the assignment was ultimately secured by the observation of the ^{34}S isotopic species. Guided by the experimentally derived rotational constants of the parent isotopologue corrected by isotope shifts derived from the CCSD(T)/cc-pCV5Z equilibrium structure, we detected 10 rotational transitions of c-C_3H_2 ^{34}S between 7 and 31 GHz (Table 2). Their intensities relative to the corresponding transitions of the parent species were consistent with the natural abundance of ^{34}S (4%). The best-fit rotational constants of c-C_3H_2 ^{34}S (Table 3) differ from those of the parent species by $\Delta B = -115.3$ MHz and $\Delta C = -90.9$ MHz, which agree with the theoretical equilibrium shifts (-115.8 and -91.5 MHz, respectively) to better than 1%. The high sensitivity of these isotopic shifts to the molecular structure leaves no doubt as to the laboratory identification of c-C_3H_2S.

Table 2
The Laboratory Rest Frequencies of c-C_3H_2S

Transition	Rest Frequency (MHz)[a]	
$J'\ K_a'\ K_c'$–$J''K_a''\ K_c''$	c-C_3H_2 ^{32}S	c-C_3H_2 ^{34}S
1 0 1–0 0 0	7697.4252	7491.2114
2 1 2–1 1 1	14931.5383	14543.5090
2 0 2–1 0 1	15389.1452	14977.3261
2 1 1–1 1 0	15857.9893	15421.1810
3 1 3–2 1 2	22393.7444	21812.0748
3 0 3–2 0 2	23069.4627	22453.2381
3 2 2–2 2 1	23091.7924	...
3 2 1–2 2 0	23114.5446	...
3 1 2–2 1 1	23783.3699	23128.5379
4 1 4–3 1 3	29851.7385	29076.8676
4 0 4–3 0 3	30732.7075	29913.8729
4 2 3–3 2 2	30784.5657	...
4 2 2–3 2 1	30841.4213	...
4 1 3–3 1 2	31704.3514	30831.9675
5 1 5–4 1 4	37304.2121	...
5 0 5–4 0 4	38373.2945	...
5 1 4–4 1 3	39619.3638	...

Notes.
[a] All frequencies have an uncertainty of 2 kHz.

Table 3
Rotational Constants of c-C_3H_2S

Parameter	c-C_3H_2 ^{32}S[a]	c-C_3H_2 ^{34}S[a]	Theory[b]
A (MHz)	32121.0(6)	32114.8(8)	32128.77
B (MHz)	4080.3272(3)	3965.0286(3)	4081.75
C (MHz)	3617.1000(3)	3526.1901(3)	3618.26
D_J (kHz)	0.519(6)	[0.519][d]	0.495
D_K (kHz)	[58.203][c]	[58.203][d]	58.203
D_{JK} (kHz)	18.34(6)	[18.34][d]	17.679
d_1 (Hz)	[−66.162][c]	[−66.162][d]	−66.162
d_2 (Hz)	[−21.459][c]	[−21.459][d]	−21.459
Transitions in fit	17	10	...
σ_{fit} (kHz)	1.7	3.4	...

Notes.
[a] The 1σ uncertainties are shown in parentheses in units of the last digit.
[b] Best-estimate theoretical ground-state rotational constants of c-C_3H_2 ^{32}S derived from the CCSD(T)/cc-pCV5Z equilibrium geometry with the CCSD(T)/cc-pCVTZ vibrational corrections (Table 1). The CD constants are the CCSD(T)/cc-pCVTZ values (Table 1).
[c] Fixed to theoretical values (Table 1).
[d] Fixed to the values of the ^{32}S species.

The full measured line list and the corresponding input and output files from SPFIT/SPCAT are provided in the .tar.gz package. The calculated rotational partition function values for c-C_3H_2S at distinct temperatures from 1 to 500 K are given in Table 4. These experimentally derived partition function values differ by only 1%–2% relative to the theoretical values reported by X. Song et al. (2022).

3. Observations

Data for this study were gathered as part of the GOTHAM survey, a comprehensive program utilizing the 100 m GBT. This analysis uses the fifth data reduction (DRV) from the GOTHAM survey, focusing on the cyanopolyyne peak (CP) in TMC-1, centered at $\alpha_{J2000} = 04^h41^m42\overset{s}{.}5$, $\delta_{J2000} = +25°41$

Table 4
Partition Function for c-C_3H_2S as Determined by SPCAT and Used in the
MCMC Analysis

Temperature (K)	Partition Function
1.0	13.1482
1.5	26.8913
2.0	43.2537
2.5	61.5061
3.0	81.3666
3.5	102.7169
4.0	125.4909
4.5	149.6359
5.0	175.1010
5.5	201.8358
6.0	229.7918
6.5	258.9228
7.0	289.1862
7.5	320.5426
8.0	352.9561
8.5	386.3935
9.375	447.2832
18.75	1261.2478
37.5	3562.1207
75.0	10069.0254
150.0	28477.5962
225.0	52326.6601
275.0	61290.6617
300.0	80582.6500
400.0	124108.0714
500.0	173475.6782

$'26.''8$. Detailed information about the data reduction procedures will be available in C. Xue et al. (2025, in preparation), while the observing strategy is described in B. A. McGuire et al. (2020). In summary, the GOTHAM survey spectra cover the C, X, Ku, K, and Ka receiver bands, providing nearly continuous coverage from 3.9 to 11.6 GHz, from 12.7 to 15.6 GHz, and from 18.0 to 36.4 GHz, totaling 29 GHz of bandwidth. All observations were made with a consistent frequency resolution of 1.4 kHz (equivalent to 0.05–0.01 km s^{-1} in velocity) and an rms noise ranging from approximately 2 to 20 mK across most of the frequency range. The rms noise varies across frequency ranges, mainly due to different total integration times and zenith opacity corrections. Data reduction involved removing radio frequency interference and artifacts, fitting the baseline continuum, and calibrating the flux density scale using the internal noise diodes. The uncertainty in flux calibration is estimated to be 10%–20%. The uncertainty of observations is computed as the quadrature sum of the local rms noise and an additional 20% systematic uncertainty.

4. Astronomical Analysis

Best-fit parameters for source size (arcsec), column density (N_T), excitation temperature (T_{ex}), line width (ΔV), and velocity with respect to the local standard of rest (v_{LSR}) were determined using a Markov Chain Monte Carlo (MCMC) fit to the data as described in R. A. Loomis et al. (2021). The advantages of the MCMC technique over a traditional least-squares approach include a more efficient exploration of a larger parameter space and direct access to the probability distributions of the parameters. This allows for a robust evaluation of parameter uncertainties and correlations, with

strongly covariant parameters manifesting as nonseparable distributions in corner plots.

For the analysis of c-C_3H_2S, a total of 52 lines are used over the entire frequency range covered by the GOTHAM survey. We follow the model assumption of four separate components with distinct systematic velocities, as revealed by recent high spectral resolution observations (K. Dobashi et al. 2018; C. Xue et al. 2020). Uniform priors were applied to the source size and N_T, while Gaussian priors were applied for T_{ex}, v_{LSR}, and ΔV (Table 5). Because of the limited range of energy levels of c-C_3H_2S transitions detected by the GOTHAM data, the prior for its T_{ex} was modeled as a Gaussian distribution centered at 4.2 K. This was derived from the posterior distribution of the well-characterized oxygen analog c-C_3H_2O (Table 9 in the Appendix), which has bright individual lines and was fitted first with uninformative uniform distributed priors, except for v_{LSR}, which was constrained by previous GOTHAM analyses (R. A. Loomis et al. 2021). The c-C_3H_2O posteriors were therefore used as priors for c-C_3H_2S for T_{ex}, v_{LSR}, and ΔV. Posterior probability distributions and covariances for each physical parameter were derived for four distinct velocity components over 30,000 iterations using 100 walkers.

To evaluate the statistical evidence that our emission model for these molecules aligns with the data, we followed the procedures detailed in R. A. Loomis et al. (2021), performing a spectral stacking and matched filtering analysis for c-C_3H_2S. Briefly, this involved computing a weighted average of the observational spectra in velocity space, centered on the observed frequency of each spectral line of the target molecule. The weights were determined by the relative intensity of the expected emission (based on spectral predictions using the MCMC-derived parameters) and the local rms noise of the observations. Due to the weak expected intensities for c-C_3H_2S, any observational windows showing emission stronger than $>5\sigma$ were excluded from the analysis to prevent interference from other species.

Simulated spectra of the molecular emission were also generated using the same MCMC-derived parameters and stacked using identical weights. This simulation served as a matched filter, passed through the observational data to produce an impulse response function. The response function quantified the statistical evidence for our emission model—and the derived molecular parameters—being consistent with the observations. The appendices of B. A. McGuire et al. (2021) complement the methodology described in R. A. Loomis et al. (2021) with an extensive analysis of its robustness, addressing the improbability of spurious signals and the minimal impact of nonthermal noise terms on the results.

Based on this analysis, we report the first interstellar detection of c-C_3H_2S toward TMC-1. Figure 1 presents the stacked observational data and the stacked MCMC model in the left panel and the matched filter response in the right panel. The statistical significance of this detection is 5.4σ as shown in the right panel of Figure 1, confirming the presence of this molecule. The posterior probability distribution for the MCMC fit is shown in Figure 5 and summarized in Table 6, suggesting a total N_T of $5.72^{+2.65}_{-1.61} \times 10^{10}$ cm^{-2} for c-C_3H_2S at an excitation temperature of $4.7^{+1.3}_{-1.1}$ K. Uncertainties, corresponding to the 16th and 84th percentiles ($\pm 1\sigma$ for a Gaussian posterior distribution), are reported for each parameter.
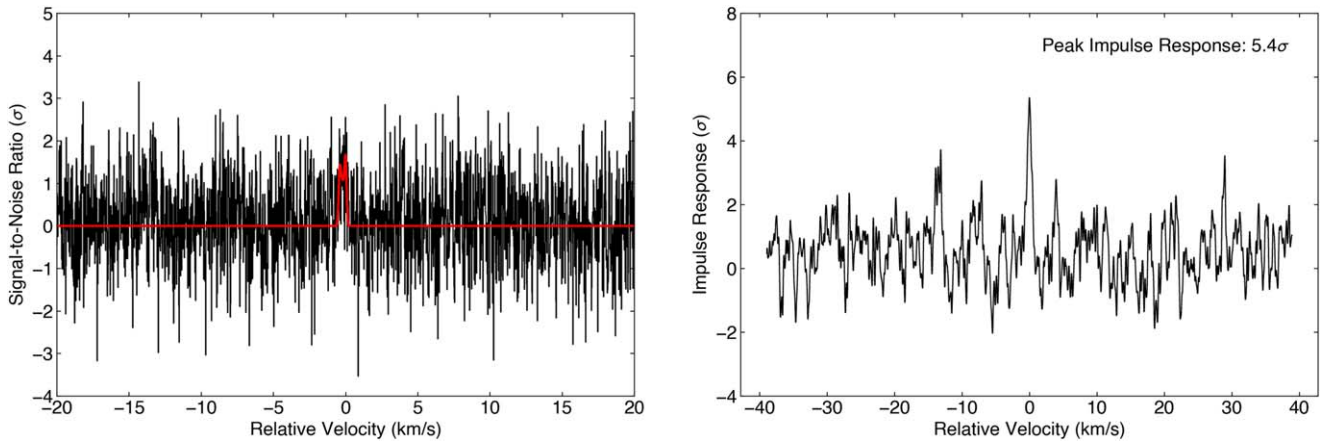
Figure 1. Velocity-stacked and matched filter spectra of c-C_3H_2S. The intensity scales are the signal-to-noise ratios (SNRs) of the response functions when centered at a given velocity. The "zero" velocity corresponds to the channel with the highest intensity to account for blended spectroscopic transitions and variations in velocity component source sizes. Velocity is relative to the systemic velocity of TMC-1 at 5.8 km s^{-1}. Left: the stacked spectra from the GOTHAM DRV data are displayed in black, overlaid with the expected line profile in red from our MCMC fit to the data. The SNR is on a per-channel basis. Right: matched filter response obtained from cross-correlating the simulated and observed velocity stacks in the left panel; the value annotated corresponds to the peak impulse response of the matched filter.

Table 5
Priors Used for MCMC Analysis of c-C_3H_2S Observations toward TMC-1

Component No.	v_{LSR} (km s^{-1})	Size (arcsec)	$\log_{10}(N_T)$ (cm^{-2})	T_{ex} (K)	ΔV (km s^{-1})
1	$N(5.624, 0.01)$	$U\{0, 300\}$	...	...	...
2	$N(5.781, 0.01)$	$U\{0, 300\}$	...	...	...
3	$N(5.915, 0.01)$	$U\{0, 300\}$	$U\{9.0, 12.0\}$	$N\{4.2, 3.0\}$	$N\{0.158, 0.05\}$
4	$N(6.018, 0.01)$	$U\{0, 300\}$	...	...	...

Note. $U\{a, b\}$ indicates a uniform distribution with minimum, a, and maximum, b, while $N(\mu, \sigma^2)$ indicates a Gaussian distribution with mean, μ, and variance, σ^2. The Gaussian priors for T_{ex}, v_{LSR}, and ΔV are informed by the posterior distribution of c-C_3H_2O.

Table 6
Summary Statistics of the Marginalized c-C_3H_2S Posterior

v_{LSR} (km s^{-1})	Size (arcsec)	N_T (10^{10} cm^{-2})	T_{ex} (K)	ΔV (km s^{-1})
$5.621^{+0.01}_{-0.01}$	148^{+103}_{-101}	$2.11^{+1.67}_{-0.86}$	...	...
$5.782^{+0.01}_{-0.01}$	146^{+105}_{-102}	$1.04^{+1.13}_{-0.73}$	...	...
$5.914^{+0.01}_{-0.01}$	151^{+102}_{-104}	$1.03^{+1.25}_{-0.75}$	$4.7^{+1.3}_{-1.1}$	$0.171^{+0.024}_{-0.024}$
$6.035^{+0.01}_{-0.01}$	158^{+95}_{-99}	$1.53^{+1.18}_{-0.88}$	...	...
N_T(Total): $5.72^{+2.65}_{-1.61} \times 10^{10}$ cm^{-2}				

In addition, for the purposes of the comparison between isomeric members, we have therefore additionally performed MCMC fittings for the other isomeric members of H_2C_3S and H_2C_3O with a spatial-separate four-component model, with results presented in detail in the Appendix. In addition to c-C_3H_2S, c-C_3H_2O and CH_2CCS are distinctly detected, whereas no clear detection of CH_2CCO or HCCCHS is made. A total N_T of $6.64^{+2.02}_{-0.71} \times 10^{11}$ cm^{-2} cm^{-2} is determined for c-C_3H_2O and $5.80^{+0.85}_{-0.61} \times 10^{11}$ cm^{-2} for CH_2CCS. Further, an upper limit of $<3.76 \times 10^{11}$ cm^{-2} is determined for CH_2CCO and $<9.51 \times 10^{11}$ cm^{-2} for HCCCHS. As shown in the Appendix, the marginal posterior for T_{ex} in c-C_3H_2O exhibits a strong correlation with column density, characterized by an elongated distribution. In contrast, the correlation between T_{ex} and N_T is less significant for CH_2CCS and c-C_3H_2S, suggesting that the observational data provide insufficient evidence to constrain the T_{ex}.

5. Discussion

The relative abundances of isomers in the ISM can provide critical astrochemical clues as to the underlying chemical reactions at play in astrophysical environments, and the detection of c-C_3H_2S reported here is no exception. As noted, the analogous C_3H_2O family of isomers—namely, cyclopropenone (c-C_3H_2O), propynal (HCCCHO), and propadienone (CH$_2$CCO)—have been the subject of a number of studies (J.-C. Loison et al. 2016; P. Gorai et al. 2024), with many focused on the curious absence of propadienone, the most thermodynamically stable of the three (R. A. Loomis et al. 2015). As was discussed in R. A. Loomis et al. (2015) and later by C. N. Shingledecker et al. (2019), the consistent nondetection of propadienone underscores the importance of kinetic factors in setting the abundances of astrochemical species in the ISM. In particular, C. N. Shingledecker et al. (2019) found from ab initio calculations that propadienone, alone among the three C_3H_2O isomers, was highly reactive with atomic hydrogen, which would thereby lower its abundance relative to the other two. Along those lines, C. N. Shingledecker et al. (2020) proposed the relative dipole principle (RDP), a kinetic rule of thumb for predicting isomer abundances. Briefly, the RDP predicts that, all other chemistry among a family of isomers being the same, the member with the smallest dipole (μ) should be the most abundant, and vice versa, since the rate of destruction via reaction with gas-phase ions is proportional to μ.

Turning our attention once more to the C_3H_2S family, we will first examine the relative abundances predicted by the RDP

Table 7
Summary of the C_3H_2O and C_3H_2S Detections toward TMC-1

Molecule	Dipole[a] (D)	ZPBE[b] (kJ mol^{-1})	N_T (10^{10} cm^{-2})	T_{ex}[c]	References
CH_2CCO	2.16	0	<37.6	[4.2]	This work
HCCCHO	2.36	22.9	728^{+408}_{-194}	$3.08^{+0.16}_{-0.12}$	A. J. Remijan et al. (2024)
c-C_3H_2O	4.39	26.3	$66.4^{+20.2}_{-7.1}$	$4.2^{+1.1}_{-0.7}$	This work
CH_2CCS	2.06	0	$58.0^{+8.5}_{-6.1}$	$11.7^{+0.9}_{-0.8}$	This work
HCCCHS	1.88	1.5	32.0	[5]	J. Cernicharo et al. (2021b)
c-C_3H_2S	4.57	11.7	$5.72^{+2.65}_{-1.61}$	$4.7^{+1.3}_{-1.1}$	This work

Notes.
[a] Value for the a-type dipole moment only.
[b] Relative zero-point bonding energy.
[c] Parameters in brackets were held fixed.

and then examine the astrochemical implications of deviations from it. To guide this discussion, the a.-type dipole moments, relative zero-point bonding energy, and total reported column densities of the C_3H_2O and C_3H_2S family of isomers are listed in Table 7. Note that the column density of HCCCHS is determined assuming a fixed excitation temperature of 5 K (J. Cernicharo et al. 2021b).

We begin by assuming dipole values of 4.57 D for c-C_3H_2S (Table 6) and 2.06 D (J. Cernicharo et al. 2021a) and 1.88 D (J. Cernicharo et al. 2021b) for CH_2CCS and HCCCHS, respectively. The RDP prediction is thus that c-C_3H_2S should be the least abundant, while HCCCHS should be slightly more abundant than CH_2CCS. As shown in Table 7, the derived column density for c-C_3H_2S is indeed the lowest relative to the other two isomers. The column densities of the other two isomers are also generally in line with the expected RDP trend, taking into account their reported uncertainties from this work and from the column density for HCCCHS reported by J. Cernicharo et al. (2021b). We note that, although C. N. Shingledecker et al. (2020) consider the RDP in light of molecular abundances in G+0.693 and Sgr B2, two sources with quite different physical conditions to TMC-1, our conclusions based on it are nevertheless still applicable here. This is because the RDP is based on an intrinsic property of reactions between ions and polar neutral molecules, which depend on the magnitude of the permanent dipole of the neutral reactant. For all such reactions, larger dipole moments result in stronger long-range forces between the reactants, which has the effect of increasing the rate coefficient. Though the degree of ionization in the Galactic center is generally higher than for TMC-1, which would result in larger overall rates, the rate coefficients thus only depend on the intrinsic properties of the species involved, and so the basic assumptions of the RDP remain valid. In this case, the agreement between the observational relative abundances and those predicted by the RDP indicates that, although the formation of c-C_3H_2S likely occurs via a different route than the other two, its overall rate of formation is likely similar to those of CH_2CCS and HCCCHS (see Section 5.1 below).

Based on the results of this analysis, two surprising outcomes emerge. First, there is a notable discrepancy in the relative column densities measured between the lowest- and highest-energy isomers of the O- and S-bearing species. Specifically, for the O-bearing molecules, the cyclic isomer exhibits a significantly higher column density than the linear isomer. In contrast, the S-bearing species display the opposite trend, with the cyclic isomer present at much lower column densities than the linear counterpart. Second, this observation highlights a striking chemical implication: as shown in C. N. Shingledecker et al. (2019), the linear form of the C_3H_2O isomer is highly reactive with atomic hydrogen in this region and in a manner that must be fundamentally different from its S-bearing analog. The reasons behind this behavior and the factors responsible for this remarkable difference in reactivity remain unknown.

5.1. Ab Initio Evaluation of a Potential Formation Route to c-C3H2S

Though a thorough study of the formation of c-C_3H_2S is beyond the scope of this work, by analogy to the c-C_3H_2O formation pathway

$$OH + c - C_3H_2 \longrightarrow H + c - C_3H_2O \qquad (1)$$
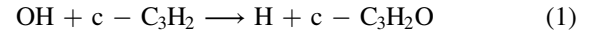
from J.-C. Loison et al. (2017), we posit that a plausible formation route for c-C_3H_2S could be

$$SH + c - C_3H_2 \longrightarrow H + c - C_3H_2S. \qquad (2)$$
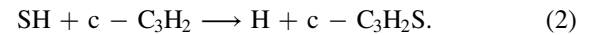
In light of this current work, we conducted an ab initio study to assess the feasibility of reaction (2).

Computational work to probe potential routes to the formation of the C_3H_2S family (c-C_3H_2S, H_2CCCS, HCCCHS) from the reaction of SH and c-C_3H_2 was carried out. This work used the M06-2X hybrid functional (Y. Zhao & D. G. Truhlar 2008) and the def2-TZVPP basis set (F. Weigend & R. Ahlrichs 2005; F. Weigend 2006), including D3 empirical dispersion corrections (S. Grimme et al. 2010) in Gaussian 09 (M. J. Frisch et al. 2009). All calculations were performed with tight convergence criteria and an ultrafine integration grid. Reactions were evaluated using relaxed scans—partial optimizations, where one coordinate corresponding to the forming bond was varied and all other coordinates were allowed to minimize. From these relaxed scans, minima were optimized and maxima were used as inputs for transition state searches. Transition states were characterized using intrinsic reaction coordinate scans to verify whether these structures connected reactants and products. Harmonic vibrational analysis was carried out on the optimized structures; the resulting frequencies and zero-point energies were scaled by 0.94985 and 0.9748,
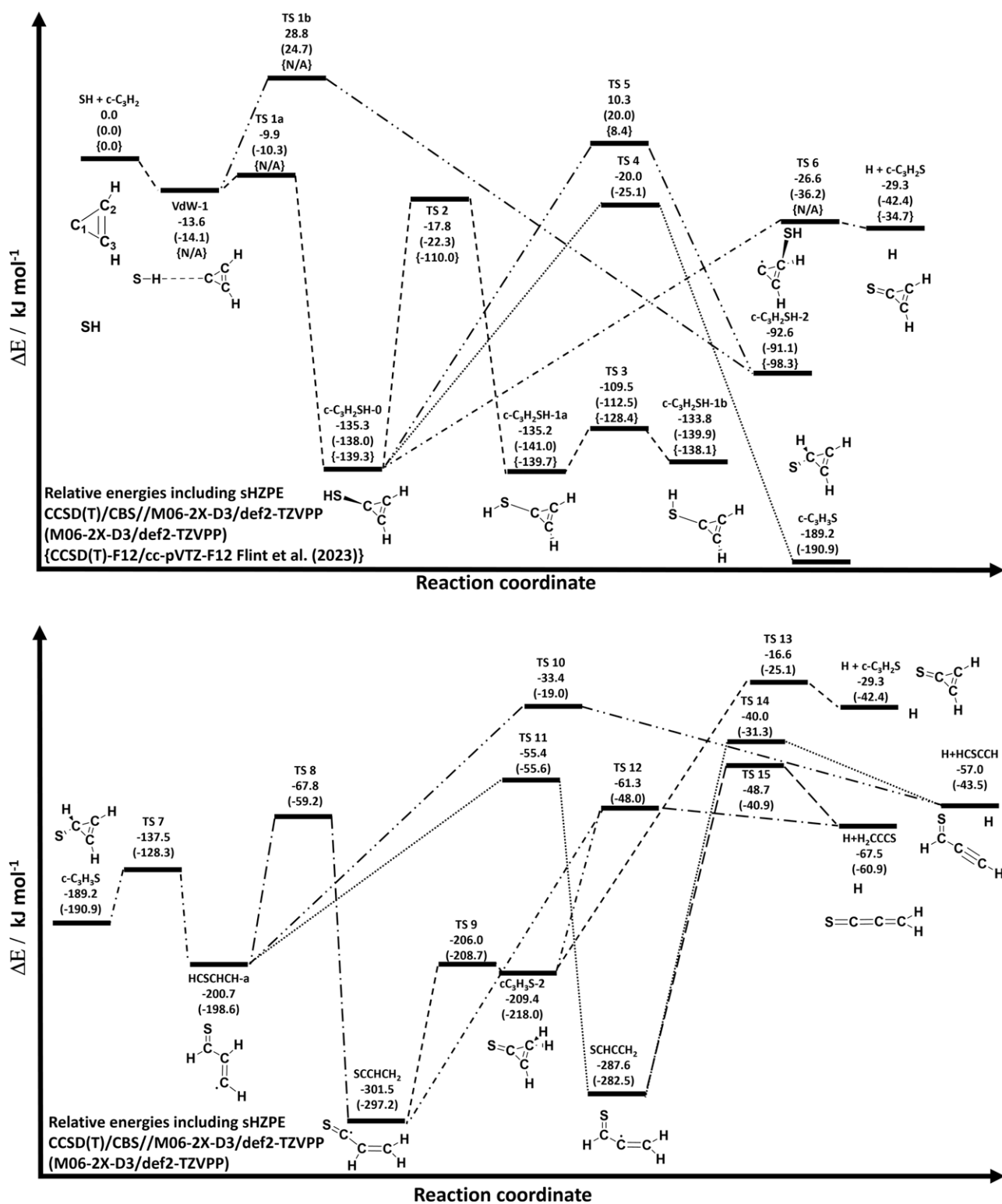
Figure 2. Potential energy surface for the reaction of SH with c-C_3H_2 at the CCSD(T)/CBS//M06-2X-D3/def2-TZVPP level; CCSD(T)-F12/cc-pVTZ-F12 values taken from A. R. Flint et al. (2023) are included. Energies are provided relative to the reactants in kJ mol^{-1} including scaled harmonic zero-point energy corrections (sHZPE). Top: summary of the initial addition of SH to the ring and prompt formation of c-C_3H_2S. Bottom: additional routes that can lead to the formation of c-C_3H_2S, HCCCHS, and CH_2CCS.

respectively, as recommended by M. K. Kesharwani et al. (2015). Single-point energies were refined by two CCSD(T) calculations using the augmented correlation-consistent basis sets aug-cc-pVDZ and aug-cc-pVTZ, with the correlation energy (CE) extrapolated to the complete basis set limit

(CE$_{CBS}$) using a modified version of the inverse power scheme taken from T. Helgaker et al. (1997) using the parameters found in F. Neese & E. F. Valeev (2011) and shown in Equation (3). The self-consistent field theory energies (SCF) were extrapolated using the exponential

scheme taken from S. Zhong et al. (2008) using the parameters found in F. Neese & E. F. Valeev (2011) and shown in Equation (4):

$$CE_{CBS} = (CE_{ADZ} \times 2^{2.46} - CE_{ATZ} \times 3^{2.46})/(2^{2.46} - 3^{2.46}) \tag{3}$$

$$SCF_{CBS} = SCF_{ATZ} + (e^{(4.42\sqrt{3} - 4.42\sqrt{2})} - 1)^{-1} \\ \times (SCF_{ATZ} - SCF_{ADZ}). \tag{4}$$

The reaction of SH with c-C_3H_2 has recently been explored by A. R. Flint & R. C. Fortenberry (2022), where the addition of SH to the ring followed by the loss of a ring-bound H atom to form c-C_3HSH was considered. These channels were found to be endothermic and have emerged barriers. In this work we considered additional channels: the loss of an H atom from the sulfonyl group, H atom transfers, and the elimination of H atoms from these intermediates and ring-opening reactions. Here addition of SH to the C1 carbon (carbon with no H atoms bound to it; see top panel of Figure 2 for its structure) of the c-C_3H_2 ring to form c-C_3H_2SH-1 (TS 1a, -9.9 kJ mol^{-1}) is followed by a submerged barrier to elimination of an H atom from the sulfonyl group (TS 6, -26.6 kJ mol^{-1}), leading to the formation of c-C_3H_2S; this channel is exothermic by 29.3 kJ mol^{-1} and is provided in the top panel of Figure 2. This channel has previously been studied at the CCSD(T)-F12/cc-pVTZ-F12 level by A. R. Flint et al. (2023), where the reaction was found to be exothermic and the initial association of SH to c-C_3H_2 to be barrierless for both ring positions. In addition, A. R. Flint et al. (2023) found the subsequent elimination of H from c-C_3H_2SH-1 to be barrierless. These values have been incorporated into Figure 2, together with the values calculated in this work. Comparing these surfaces, aside from the barrierless pathways, the barrier to interconversion between the bent and planar forms of c-C_3H_2SH-1 calculated here differs markedly from that found by A. R. Flint et al. (2023); however, both barriers are significantly submerged compared to the reactant asymptote. Aside from these differences, the two surfaces are in excellent agreement typically differing by only 1 kcal mol^{-1}. The current surface also considers additional submerged channels, following H atom transfer from the sulfonyl group to the ring, and subsequent ring-opening reactions can lead to the formation of both H_2CCCS and $HCCCHS$; a subset of the lowest-energy pathways found are presented in the bottom panel of Figure 2.

The addition of SH to the c-C_3H_2 ring at the C2 position (the carbons with an H atom bound to them) leads to the formation of c-C_3H_2SH-2, which, following H atom elimination from the sulfonyl group, leads to the formation of $HCCCHS$. H atom transfer (TS 5) allows for the formation of c-C_3H_2SH-1 with the same channels. However, all these channels require the initial addition process to occur, and this appears to require surmounting an emerged barrier in the entrance channel (TS 1b, 28.8 kJ mol^{-1}); therefore, it is likely that the predominant reaction from SH and c-C_3H_2 is via addition at C1.

This theoretical study highlights the potential of the reaction between SH and c-C_3H_2 to produce three isomers of C_3H_2S. Among these pathways, the formation of the cyclic isomer c-C_3H_2S is likely to be the preferred channel, due to the presence of a submerged barrier for H atom elimination following the initial addition step. Further theoretical and experimental work is required to evaluate the kinetics and product branching ratio of this reaction under conditions relevant to TMC-1.

6. Conclusions

We report the spectroscopic characterization of cyclopropenethione (c-C_3H_2S) in both laboratory experiments and astronomical observations, culminating in its detection using the GBT as part of the GOTHAM large program. This discovery marks the completion of the C_3H_2S isomeric family in TMC-1, as the other two isomers, CH_2CCS and $HCCCHS$, were previously identified in the same source. Adding to the intriguing discoveries of sulfur-bearing species in TMC-1, the total column density of c-C_3H_2S is reported as $5.72^{+2.65}_{-1.61} \times 10^{10}$ cm^{-2} at an excitation temperature of $4.7^{+1.3}_{-1.1}$ K—considerably lower than the reported column densities of both CH_2CCS and $HCCCHS$. This finding aligns with the RDP, a kinetic heuristic that predicts the most abundant isomer in a family to be the one with the smallest dipole moment assuming similar underlying chemistry. However, for the O-bearing molecules, the cyclic isomer exhibits a significantly *higher* column density than the linear isomer. As such, the linear form of the C_3H_2O isomer, which is highly reactive with atomic hydrogen in this region, must react in a fundamentally different way from its isovalent S-bearing analog. Overall, the RDP is now consistent between both the sulfur- and oxygen-bearing isomer families in TMC-1, although the reasons behind the behavior and the factors responsible for this remarkable difference in reactivity between the linear species remain unknown.

7. Data Access and Code

The code used to perform the analysis is part of the `molsim` open-source package (B. A. McGuire et al. 2024).

Facilities: GBT.

Appendix
MCMC Fitting Results

We have fit c-C_3H_2O, c-C_3H_2S, CH_2CCS, CH_2CCO, and $HCCCHS$ using MCMC fits to the GOTHAM observations. Four emission features of c-C_3H_2O are well detected above the noise, as shown in Figure 3. The adopted prior probability distributions for each parameter are detailed in Table 8. The priors for v_{LSR} of the four components are chosen to be a Gaussian distribution centered at approximately 5.6, 5.8, 5.9, and 6.0 km s^{-1}, informed by previous GOTHAM analyses (R. A. Loomis et al. 2021). Meanwhile, all the remaining parameters have uninformative uniformly distributed priors. A corner plot of the posterior probability distributions and parameter covariances for the c-C_3H_2O fit is shown in Figure 4, with statistics of the marginalized posterior summarized in Table 9. We adopt the 50th percentile value of the posterior probability distributions as the representative value of each parameter to construct composite line profiles, as shown in Figure 3.

In order to achieve self-consistency, we adopted the same prior probability distributions for c-C_3H_2S and CH_2CCS, informed by the posterior distribution of c-C_3H_2O. The specific prior probability distributions for each parameter are detailed in Table 5. A corner plot of the parameter covariances and their

distribution for the c-C_3H_2S MCMC fit is shown in Figure 5. An identical analysis to that for c-C_3H_2S was carried out for CH_2CCS, with a total of 36 transitions being considered for the MCMC fitting. The resulting posterior probability distributions for the CH_2CCS fit are shown in Figure 6, with statistics of the marginalized posterior summarized in Table 10. The majority of CH_2CCS emission is contributed by three of the four velocity components, a behavior similarly observed in other molecules toward TMC-1, such as propargyl cyanide and E-1-cyano-1,3-butadiene (B. A. McGuire et al. 2020; I. R. Cooke et al. 2023). There is not a significant detection in the component with a v_{LSR} of 5.92 km s^{-1}. However, both four-component and three-component models result in similar total column densities. For consistency, we thereby present only the results assuming a four-velocity-component model.

From the GOTHAM observations that were processed as part of DRV, no signal beyond a 1σ detection limit can be assigned to CH_2CCO and $HCCCHS$. Column density upper limits are therefore constrained using the modified fitting process (R. A. Loomis et al. 2016). Source sizes, T_{ex}, v_{LSR}, and ΔV were held fixed to the 50th percentile value in c-C_3H_2O posteriors. Corner plots of column densities for CH_2CCO and $HCCCHS$ are shown in Figure 7. Upper limits are given as the 97.8th percentile (2σ) value in Table 11.
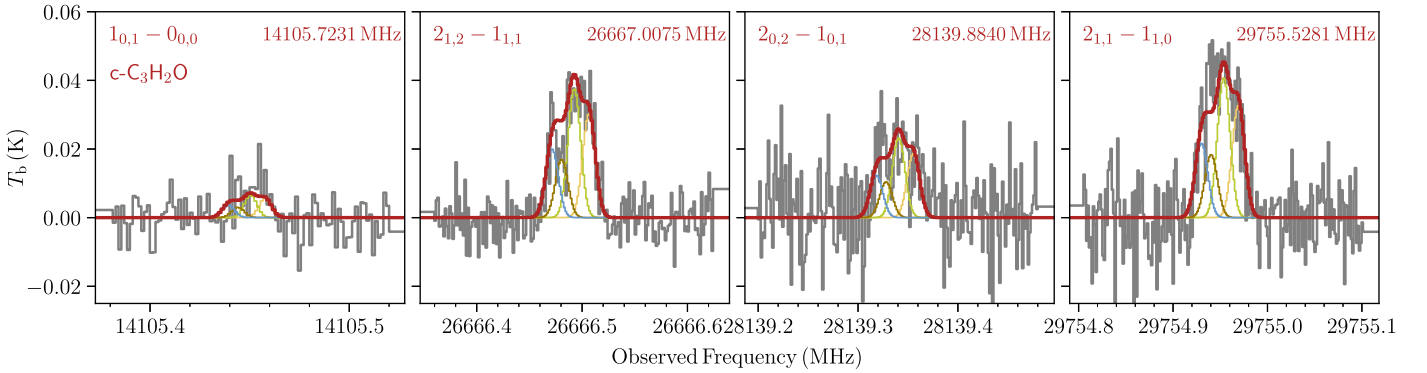

Figure 3. Individual line detections of c-C_3H_2O transitions in the GOTHAM DRV data. The observed spectra are displayed in black, while the best-fitting model to the data, including all velocity components, is overlaid in red. Simulated spectra of the individual velocity components are shown in yellow (5.62 km s^{-1}), lime (5.78 km s^{-1}), brown (5.92 km s^{-1}), and blue (6.02 km s^{-1}). See Table 9.

Table 8
Priors Used for MCMC Analysis of c-C_3H_2O Observations toward TMC-1

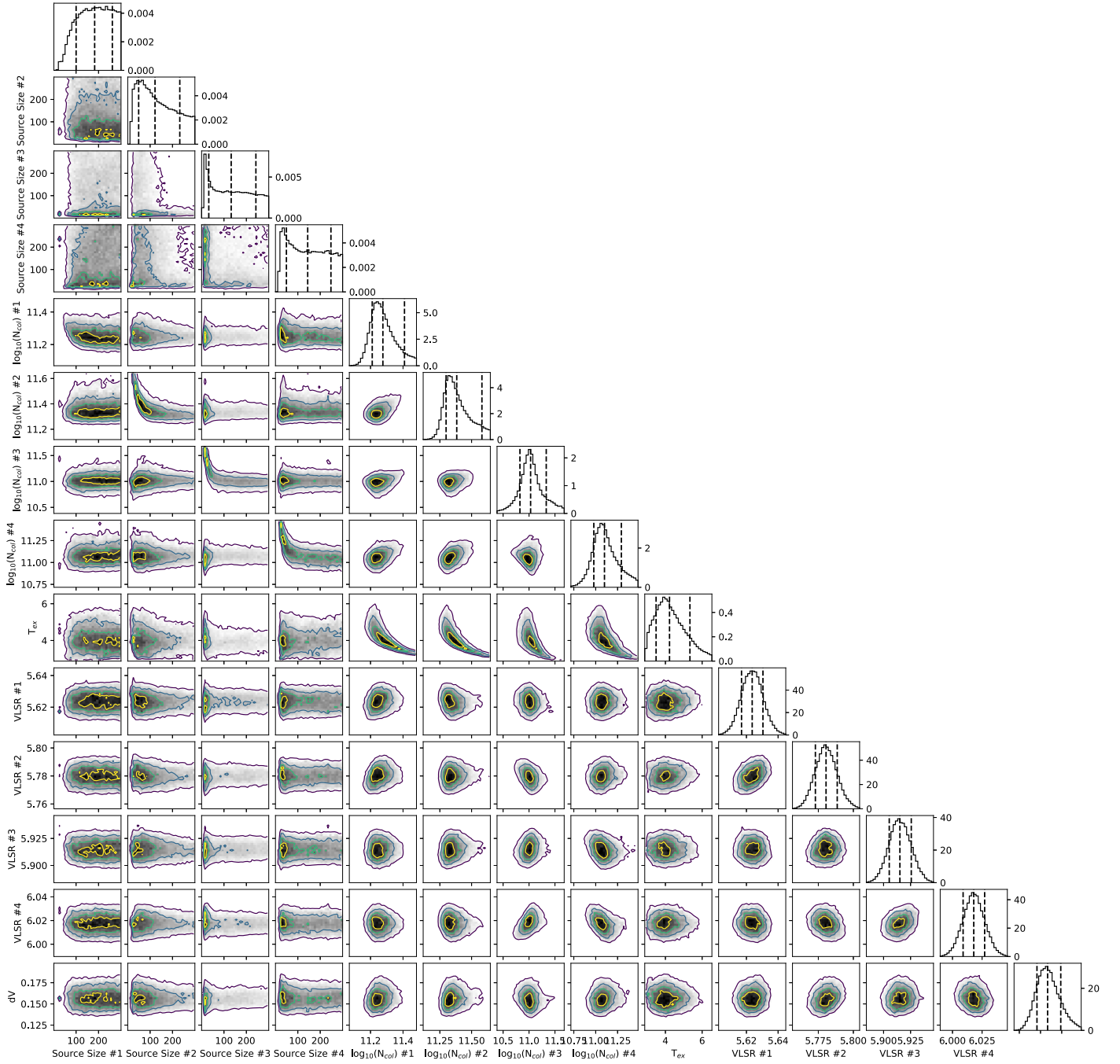| Component No.	v_{LSR} (km s^{-1})	Size (arcsec)	$\log_{10}(N_T)$ (cm^{-2})	T_{ex} (K)	ΔV (km s^{-1})
1	$N(5.624, 0.01)$	$U\{0, 300\}$	...	...	...
2	$N(5.790, 0.01)$	$U\{0, 300\}$	$U\{10.0, 12.0\}$	$U\{2.73, 15.0\}$	$U\{0.1, 0.3\}$
3	$N(5.910, 0.01)$	$U\{0, 300\}$	...	...	...
4	$N(6.033, 0.01)$	$U\{0, 300\}$	...	...	...

Figure 4. Parameter covariances and marginalized posterior distributions for the c-C_3H_2O MCMC fit. The 16th, 50th, and 84th confidence intervals (corresponding to $\pm 1\sigma$ for a Gaussian posterior distribution) are shown as vertical lines.

Table 9
Summary Statistics of the Marginalized c-C_3H_2O Posterior

v_{LSR} (km s^{-1})	Size (arcsec)	N_T (10^{10} cm^{-2})	T_{ex} (K)	ΔV (km s^{-1})
$5.624^{+0.007}_{-0.007}$	183^{+79}_{-83}	$1.89^{+0.68}_{-0.26}$	...	...
$5.781^{+0.008}_{-0.008}$	122^{+111}_{-73}	$2.42^{+1.40}_{-0.42}$	$4.2^{+1.1}_{-0.7}$	$0.158^{+0.015}_{-0.013}$
$5.915^{+0.011}_{-0.010}$	132^{+110}_{-100}	$1.07^{+1.08}_{-0.40}$	...	...
$6.018^{+0.009}_{-0.009}$	144^{+104}_{-95}	$1.26^{+0.70}_{-0.31}$	...	...
N_T(Total): $6.64^{+2.02}_{-0.71} \times 10^{11}$ cm^{-2}				

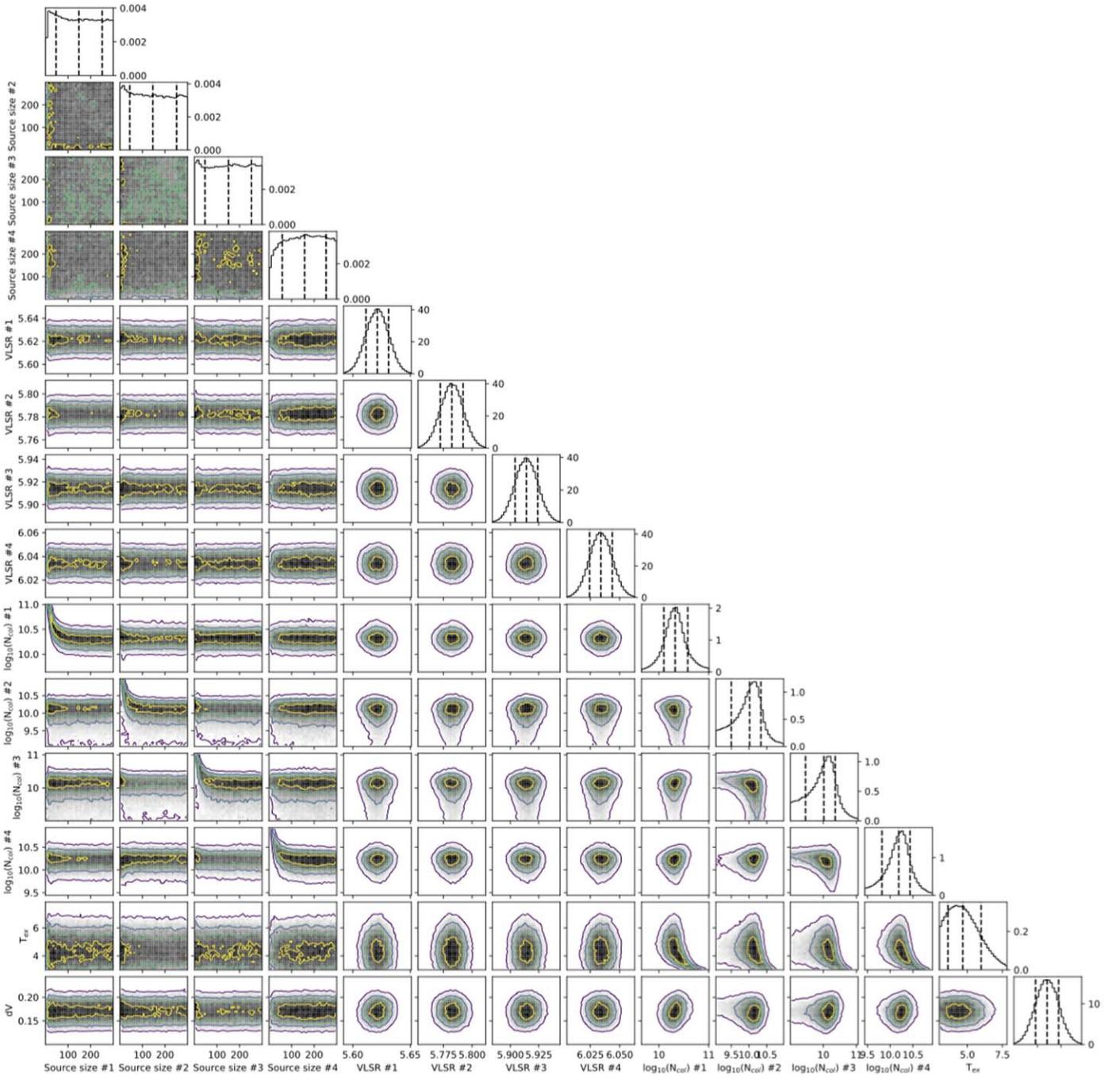**Note.** Uncertainties of total N_T are derived by adding the uncertainties of the individual components in quadrature.

Figure 5. Parameter covariances and marginalized posterior distributions for the c-C_3H_2S MCMC fit. The 16th, 50th, and 84th confidence intervals (corresponding to $\pm 1\sigma$ for a Gaussian posterior distribution) are shown as vertical lines.
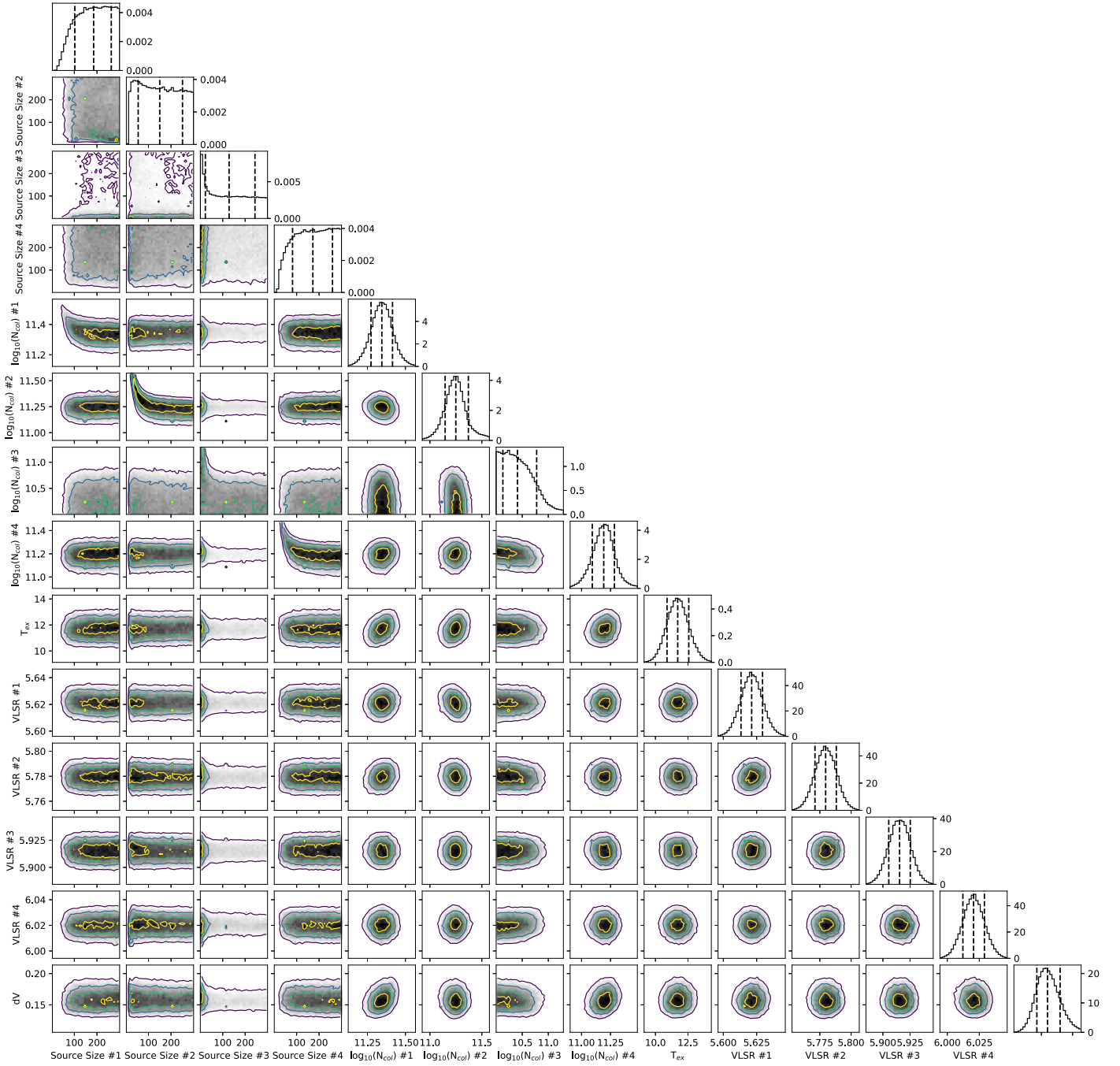
Figure 6. Parameter covariances and marginalized posterior distributions for the CH$_2$CCS MCMC fit. The 16th, 50th, and 84th confidence intervals (corresponding to ±1σ for a Gaussian posterior distribution) are shown as vertical lines.

Table 10
Summary Statistics of the Marginalized CH$_2$CCS Posterior

v_{LSR} (km s^{-1})	Size (arcsec)	N_T (10^{10} cm^{-2})	T_{ex} (K)	ΔV (km s^{-1})
$5.621^{+0.008}_{-0.008}$	185^{+78}_{-83}	$2.21^{+0.39}_{-0.34}$	⋯	⋯
$5.780^{+0.009}_{-0.009}$	150^{+101}_{-96}	$1.78^{+0.57}_{-0.37}$	⋯	⋯
$5.915^{+0.010}_{-0.010}$	128^{+116}_{-106}	$0.26^{+0.34}_{-0.12}$	$11.7^{+0.9}_{-0.8}$	$0.160^{+0.020}_{-0.017}$
$6.020^{+0.008}_{-0.008}$	172^{+88}_{-91}	$1.55^{+0.37}_{-0.32}$	⋯	⋯
N_T(Total): $5.80^{+0.85}_{-0.61} \times 10^{11}$ cm^{-2}				

Note. Uncertainties of total N_T are derived by adding the uncertainties of the individual components in quadrature.
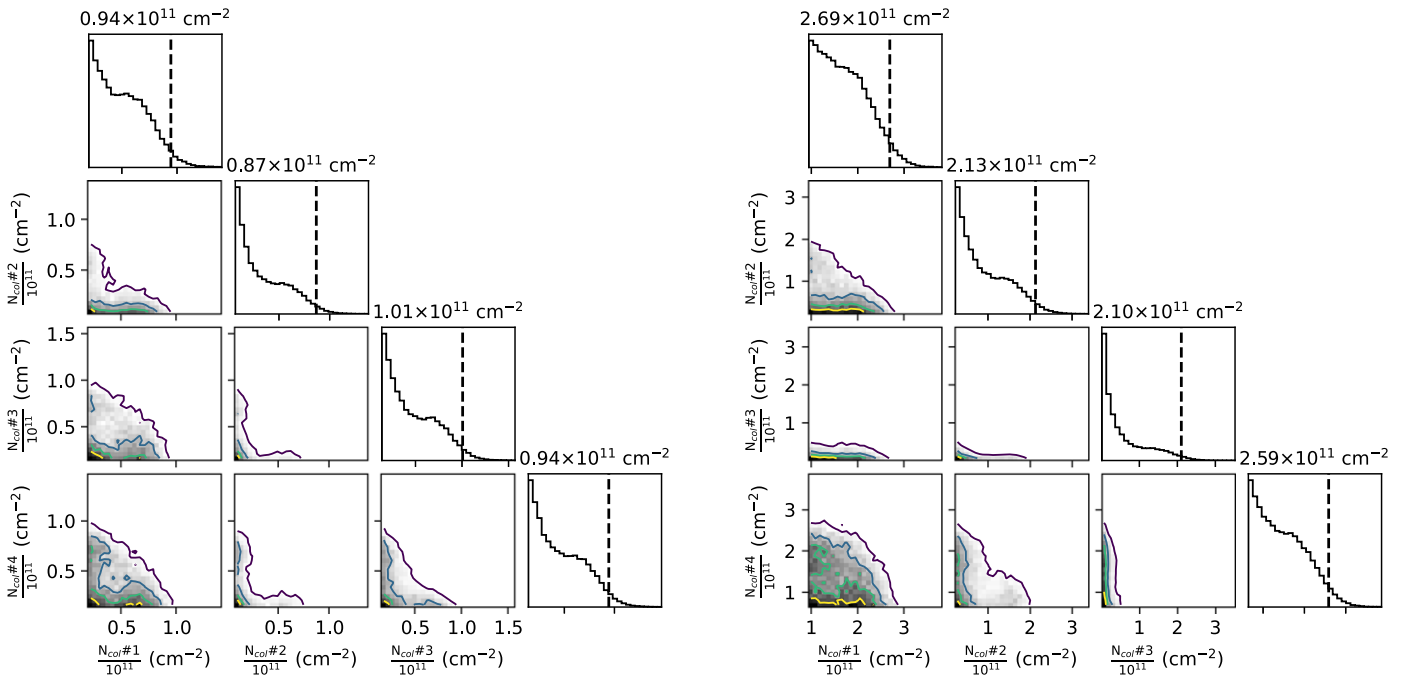
Figure 7. Marginalized posterior distributions of column densities for the H$_2$CCCO MCMC fit (left panel) and the HCCCHS MCMC fit (right panel). The 97.8th confidence intervals are shown as vertical lines.

Table 11
Summary Statistics of the Marginalized CH$_2$CCO and HCCCHS Posterior

v_{LSR} (km s^{-1})	Size (arcsec)	T_{ex} (K)	ΔV (km s^{-1})	CH$_2$CCO N_T (10^{11} cm^{-2})	HCCCHS N_T (10^{11} cm^{-2})
[5.624]	[183]	…	…	<0.94	<2.69
[5.781]	[122]	…	…	<0.87	<2.13
[5.915]	[132]	[4.2]	[0.158]	<1.01	<2.10
[6.018]	[144]	…	…	<0.94	<2.59

CH$_2$CCO N_T(Total): <3.76 × 10^{11} cm^{-2}
HCCCHS N_T(Total): <9.51 × 10^{11} cm^{-2}

ORCID iDs

Anthony J. Remijan ⓘ https://orcid.org/0000-0001-9479-9287
P. Bryan Changala ⓘ https://orcid.org/0000-0003-0304-9814
Ci Xue ⓘ https://orcid.org/0000-0003-2760-2119
Elsa Q. H. Yuan ⓘ https://orcid.org/0009-0000-4968-3779
Haley N. Scolati ⓘ https://orcid.org/0000-0002-8505-4459
Christopher N. Shingledecker ⓘ https://orcid.org/0000-0002-5171-7568
Thomas H. Speak ⓘ https://orcid.org/0000-0001-8134-5681
Ilsa R. Cooke ⓘ https://orcid.org/0000-0002-0850-7426
Ryan Loomis ⓘ https://orcid.org/0000-0002-8932-1219
Andrew M. Burkhardt ⓘ https://orcid.org/0000-0003-0799-0927
Zachary T. P. Fried ⓘ https://orcid.org/0000-0001-5020-5774
Gabi Wenzel ⓘ https://orcid.org/0000-0002-0332-2641
Andrew Lipnicky ⓘ https://orcid.org/0000-0002-6667-7773
Michael C. McCarthy ⓘ https://orcid.org/0000-0001-9142-0008
Brett A. McGuire ⓘ https://orcid.org/0000-0003-1254-4817

References

Artur de la Villarmois, E., Guzmán, V. V., Yang, Y. L., Zhang, Y., & Sakai, N. 2023, A&A, 678, A124
Asplund, M., Grevesse, N., & Sauval, A. J. 2005, in ASP Conf. Ser. 336, Cosmic Abundances as Records of Stellar Evolution and Nucleosynthesis, ed. I. Barnes, G. Thomas, & F. N. Bash (San Francisco, CA: ASP), 25
Bartlett, R. J., Watts, J., Kucharski, S., & Noga, J. 1990, CPL, 165, 513
Brown, R. D., Dyall, K. G., Elmes, P. S., Godfrey, P. D., & McNaughton, D. 1988, JAChS, 110, 789
Brown, R. D., Godfrey, P., Champion, R., & Woodruff, M. 1982, AJCh, 35, 1747
Cernicharo, J., Agúndez, M., Cabezas, C., et al. 2022, EPJWC, 265, 00041
Cernicharo, J., Cabezas, C., Agúndez, M., et al. 2021a, A&A, 648, L3
Cernicharo, J., Cabezas, C., Endo, Y., et al. 2021b, A&A, 650, L14
Charnley, S. B. 1997, ApJ, 481, 396
Cooke, I. R., Xue, C., Changala, P. B., et al. 2023, ApJ, 948, 133
Crabtree, K. N., Martin-Drumel, M.-A., Brown, G. G., et al. 2016, JChPh, 144, 124201
Dobashi, K., Shimoikura, T., Nakamura, F., et al. 2018, ApJ, 864, 82
Dunning, T. H. 1989, JChPh, 90, 1007
Esplugues, G. B., Viti, S., Goicoechea, J. R., & Cernicharo, J. 2014, A&A, 567, A95
Flint, A. R., & Fortenberry, R. C. 2022, ApJ, 938, 15
Flint, A. R., Rogers, B. N., & Fortenberry, R. C. 2023, MNRAS, 522, 4215
Frisch, M. J., Trucks, G. W., Schlegel, H. B., et al. 2009, Gaussian 09 Revision D.01
Fuente, A., Rivière-Marichalar, P., Beitia-Antero, L., et al. 2023, A&A, 670, A114
Gerin, M., Liszt, H., Pety, J., & Faure, A. 2024, A&A, 686, A49
Gorai, P., Law, C.-Y., Tan, J. C., et al. 2024, ApJ, 960, 127
Gordon, V. D., McCarthy, M. C., Apponi, A. J., & Thaddeus, P. 2001, ApJS, 134, 311

Gordon, V. D., McCarthy, M. C., Apponi, A. J., & Thaddeus, P. 2002, ApJS, 138, 297

Grabow, J. U., Palmer, E. S., McCarthy, M. C., & Thaddeus, P. 2005, RScI, 76, 093106

Grimme, S., Antony, J., Ehrlich, S., & Krieg, H. 2010, JChPh, 132, 154104

Helgaker, T., Klopper, W., Koch, H., & Noga, J. 1997, JChPh, 106, 9639

Hollis, J. M., Remijan, A. J., Jewell, P. R., & Lovas, F. J. 2006, ApJ, 642, 933

Howk, J. C., Sembach, K. R., & Savage, B. D. 2006, ApJ, 637, 333

Irvine, W. M., Brown, R. D., Cragg, D. M., et al. 1988, ApJL, 335, L89

Kesharwani, M. K., Brauer, B., & Martin, J. M. L. 2015, JPCA, 119, 1701

Lee, K. L. K., Martin-Drumel, M.-A., Lattanzi, V., et al. 2019, MolPh, 117, 1381

Lee, T. J., & Rendell, A. P. 1991, JChPh, 94, 6229

Loison, J.-C., Agúndez, M., Marcelino, N., et al. 2016, MNRAS, 456, 4101

Loison, J.-C., Agúndez, M., Wakelam, V., et al. 2017, MNRAS, 470, 4075

Loomis, R. A., Burkhardt, A. M., Shingledecker, C. N., et al. 2021, NatAs, 5, 188

Loomis, R. A., McGuire, B. A., Shingledecker, C., et al. 2015, ApJ, 799, 34

Loomis, R. A., Shingledecker, C. N., Langston, G., et al. 2016, MNRAS, 463, 4175

Matthews, D. A., Cheng, L., Harding, M. E., et al. 2020, JChPh, 152, 214108

McCarthy, M. C., Cooksy, A. L., Mohamed, S., Gordon, V. D., & Thaddeus, P. 2003, ApJS, 144, 287

McCarthy, M. C., Lee, K. L. K., Porterfield, J. P., Changala, P. B., & Eckhardt, A. K. 2021, MolPh, 119, e1975052

McGuire, B. A., Burkhardt, A. M., Loomis, R. A., et al. 2020, ApJL, 900, L10

McGuire, B. A., Loomis, R. A., Burkhardt, A. M., et al. 2021, Sci, 371, 1265

McGuire, B. A., Martin-Drumel, M.-A., Lee, K. L. K., et al. 2018, PCCP., 20, 13870

McGuire, B. A., Xue, C., Lee, K. L. K., El-Abd, S., & Loomis, R. A. 2024, molsim, v0.5.0, Zenodo, doi:10.5281/zenodo.12697227

Mills, I. M. 1972, in Molecular Spectroscopy: Modern Research, ed. K. N. Rao & C. W. Mathews (New York: Academic Press), 115

Neese, F., & Valeev, E. F. 2011, JCTC, 7, 33

Peterson, K. A., & Dunning, T. H. 2002, JChPh, 117, 10548

Raghavachari, K., Trucks, G. W., Pople, J. A., & Head-Gordon, M. 1989, CPL, 157, 479

Remijan, A. J., Fried, Z. T. P., Cooke, I. R., et al. 2024, ApJ, 976, 105

Ruffle, D. P., Hartquist, T. W., & Caselli, P. 1999, MNRAS, 306, 691

Shingledecker, C. N., Álvarez Barcia, S., Korn, V. H., & Kästner, J. 2019, ApJ, 878, 80

Shingledecker, C. N., Molpeceres, G., Rivilla, V. M., Majumdar, L., & Kner, J. 2020, ApJ, 897, 158

Song, X., Wang, M., Yang, C., et al. 2022, Comput. Theor. Chem., 1217, 113877

Stanton, J. F., Gauss, J., Cheng, L., et al. 2020, CFOUR, Coupled-cluster Techniques for Computational Chemistry, a Quantum-chemical Program Package

Stäuber, P., Doty, S. D., van Dishoeck, E. F., & Benz, A. O. 2005, A&A, 440, 949

Tychoniec, Ł., van Dishoeck, E. F., van't Hoff, M. L. R., et al. 2021, A&A, 655, A65

Vidal, T. H. G., Loison, J-C., & Jaziri, A. Y. 2017, MNRAS, 469, 435

Weigend, F. 2006, PCCP, 8, 1057

Weigend, F., & Ahlrichs, R. 2005, PCCP, 7, 3297

Woon, D. E., & Dunning, T. H. 1995, JChPh, 103, 4572

Xue, C., Remijan, A. J., Burkhardt, A. M., & Herbst, E. 2019, ApJ, 871, 112

Xue, C., Willis, E. R., Loomis, R. A., et al. 2020, ApJL, 900, L9

Yocum, K. M., Wilkins, O. H., Bardwell, J. C., Milam, S. N., & Gerakines, P. A. 2023, ApJL, 958, L41

Zhao, Y., & Truhlar, D. G. 2008, JTCA, 120, 215

Zhong, S., Barnes, E. C., & Petersson, G. A. 2008, JChPh, 129, 184116

Zhou, S., Evans, N. J. I., Koempe, C., & Walmsley, C. M. 1993, ApJ, 404, 232